JACS
JOURNAL OF THE AMERICAN CHEMICAL SOCIETY
pubs.acs.org/JACS
Article

Bottom-Up Construction of Metal–Organic Framework Loricae on Metal Nanoclusters with Consecutive Single Nonmetal Atom Tuning for Tailored Catalysis

Qing You,[‖] He Wang,[‖] Yan Zhao,[‖] Wentao Fan,[‖] Wanmiao Gu, Hai-Long Jiang,* and Zhikun Wu*

Cite This: J. Am. Chem. Soc. 2024, 146, 9026–9035

Read Online

ACCESS | Metrics & More | Article Recommendations | Supporting Information

ABSTRACT: The introduction of single or multiple heterometal atoms into metal nanoparticles is a well-known strategy for altering their structures (compositions) and properties. However, surface single nonmetal atom doping is challenging and rarely reported. For the first time, we have developed synthetic methods, realizing "surgery"-like, successive surface single nonmetal atom doping, replacement, and addition for ultrasmall metal nanoparticles (metal nanoclusters, NCs), and successfully synthesized and characterized three novel bcc metal NCs $Au_{38}I(S\text{-}Adm)_{19}$, $Au_{38}S(S\text{-}Adm)_{20}$, and $Au_{38}IS(S\text{-}Adm)_{19}$ (S-Adm: 1-adamantanethiolate). The influences of single nonmetal atom replacement and addition on the NC structure and optical properties (including absorption and photoluminescence) were carefully investigated, providing insights into the structure (composition)–property correlation. Furthermore, a bottom-up method was employed to construct a metal–organic framework (MOF) on the NC surface, which did not essentially alter the metal NC structure but led to the partial release of surface ligands and stimulated metal NC activity for catalyzing *p*-nitrophenol reduction. Furthermore, surface MOF construction enhanced NC stability and water solubility, providing another dimension for tunning NC catalytic activity by modifying MOF functional groups.

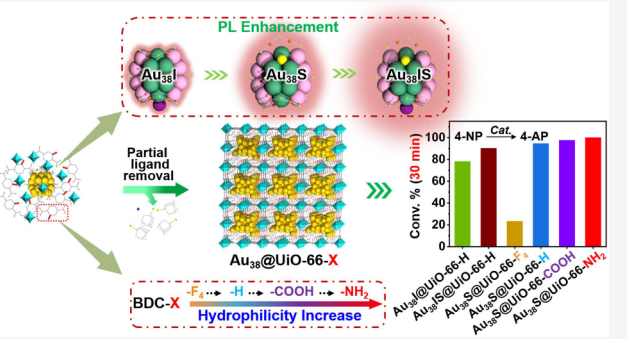

INTRODUCTION

Metal nanoclusters (NCs, ultrasmall metal nanoparticles) have attracted increasing interest in recent years partly due to their tunability with atomic precision.[1−6] Metal atom doping has been widely employed for tailoring the physicochemical properties of metal NCs and enabling the composition (structure)–property correlation.[7−14] However, surface nonmetal atom introduction, especially "surgery"-like single nonmetal atom doping, replacement, or addition, is challenging owing to the control difficulties.[15−23] To the best of our knowledge, surface single nonmetal atom replacement, not to mention successive surface single nonmetal atom doping, replacement, and addition, has not been previously reported. Unlike thiols and phosphines, single nonmetal atoms such as sulfur and halogen can provide more room for access by the substrates and thus facilitate catalytic reactions;[24−28] nevertheless, single nonmetal atoms might not protect NCs from attack as well as thiols or phosphines. To counteract the negative effect of surface single nonmetal atom occupation on NC stability, one strategy is to construct loricae for enhanced protection of the metal NCs. As such, metal–organic frameworks (MOFs) are ideal candidates since they have well-defined and tunable pore structures,[29−31] which not only protect metal NCs from attack but also leave room for reaction, providing pathways for substance transport, and so forth.[32−38] Notably, MOF introduction can also alter the hydrophilicity of metal NCs, as we previously reported, which enables hydrophobic metal NCs to catalyze reactions in the aqueous phase.[39] The introduction of MOF loricae on metal NCs has been reported and generally conducted by mixing MOFs with metal NCs.[39−43] In this complex strategy, the size match between the MOF cavity and the metal NC should be considered, or else the encapsulation can not be well conducted. An alternative complexing strategy is the bottom-up construction of a MOF lorica on a template-like metal NC surface based on the self-adaptation of metal NCs and MOF loricae.[41,44−50] However, such a complexing mode has rarely been reported, and calcination of the resulting composites is generally adopted before their use as catalysts.[41,44,45,47,48] Under this circumstance, it remains unclear whether there are some modifications on the metal NCs surface during MOF lorica formation. This study was inspired by these interesting

Received: December 4, 2023
Revised: February 13, 2024
Accepted: February 16, 2024
Published: March 5, 2024

https://doi.org/10.1021/jacs.3c13635
J. Am. Chem. Soc. 2024, 146, 9026–9035

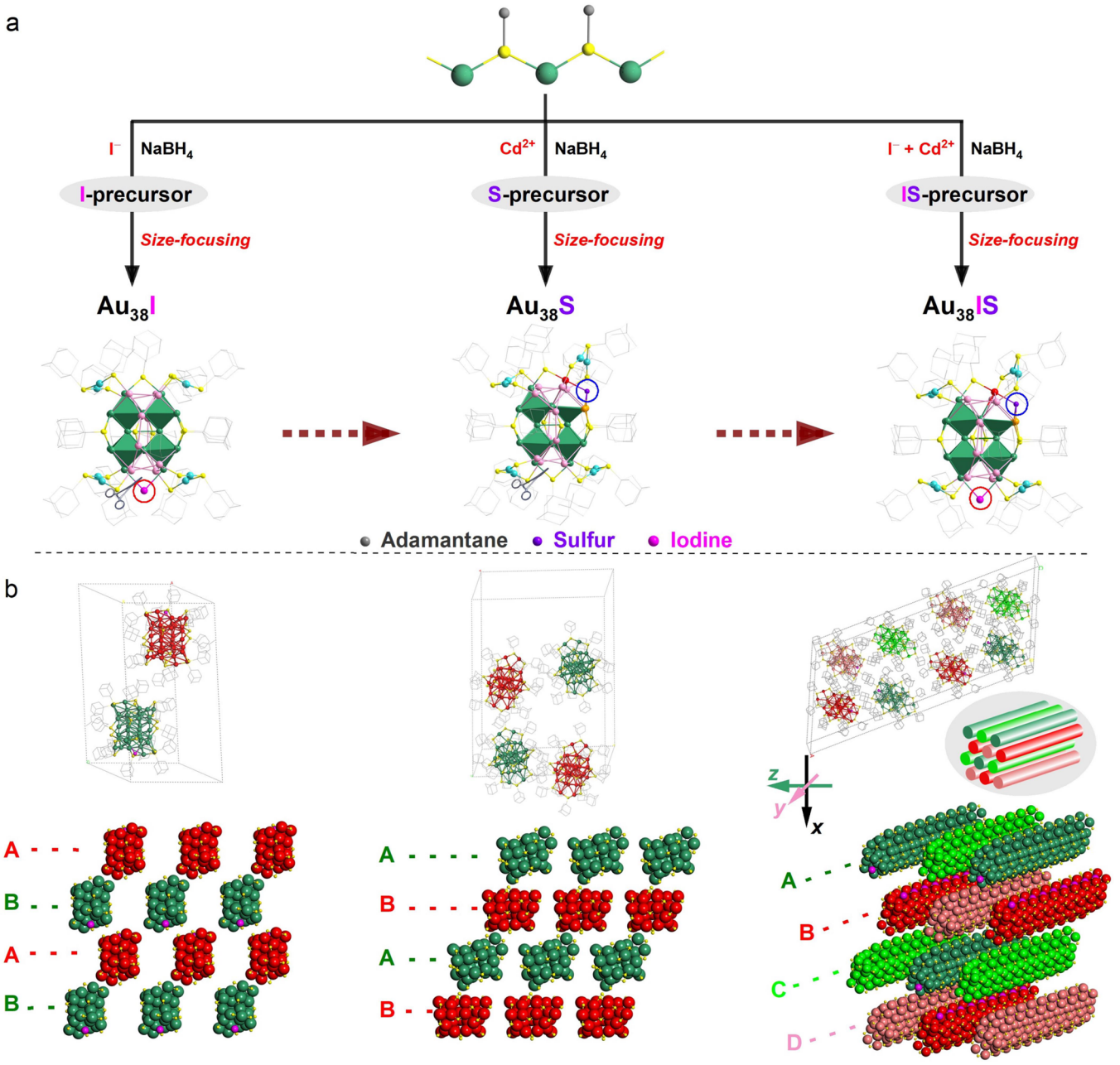

Figure 1. Synthesis (a) and crystallographic arrangement (b) of $Au_{38}I$, $Au_{38}S$, and $Au_{38}IS$. Note that, all C and H atoms are omitted in (b) for clarity.

issues, including the aforementioned challenging single nonmetal atom "surgery". Our strategy is detailed below.

RESULTS AND DISCUSSION

Syntheses and Structural Analyses of Three Au_{38} NCs. Gold NCs were selected as the investigated NCs due to their relative stability compared to silver and other metal NCs. 1-Adamantanethiol (Adm-SH) was selected as the protecting ligand for its bulkiness and rigidity, which may leave room for single atom coating on the surface of gold NCs and also produce single sulfur atoms well after thermal cracking.[17,51,52] Iodine (I) and sulfur (S) were selected as the incoming single nonmetal atoms, given that they have good affinity with gold and can be easily provided by salt and thiol, respectively. Specifically, KI and Adm-SH were employed as the precursors of I and S, respectively. Interestingly, it was found that the addition of Cd^{2+} could accelerate the production of S, thus $Cd(NO_3)_2{\cdot}4H_2O$ was added during the synthesis of S-enclosed gold NCs. Considering that Au−thiol interaction is generally stronger than Au−S complexing,[20,21,53,54] we conjectured that acid addition might weaken the Au−thiol interaction and facilitate controlled S occupation, which was confirmed experimentally. Therefore, nitric acid was added as a mediator in all of the syntheses. As shown in Figure 1a, the single I-doped gold NC $Au_{38}I(S\text{-}Adm)_{19}$ ($Au_{38}I$ for short) was synthesized by a typical two-step synthesis method with the addition of KI and some parameter modifications. Subsequently, the single S-doped gold NC $Au_{38}S(S\text{-}Adm)_{20}$ ($Au_{38}S$ for short) was synthesized by replacing KI with $Cd(NO_3)_2{\cdot}4H_2O$ (see the Methods for the experimental

https://doi.org/10.1021/jacs.3c13635
J. Am. Chem. Soc. 2024, 146, 9026−9035

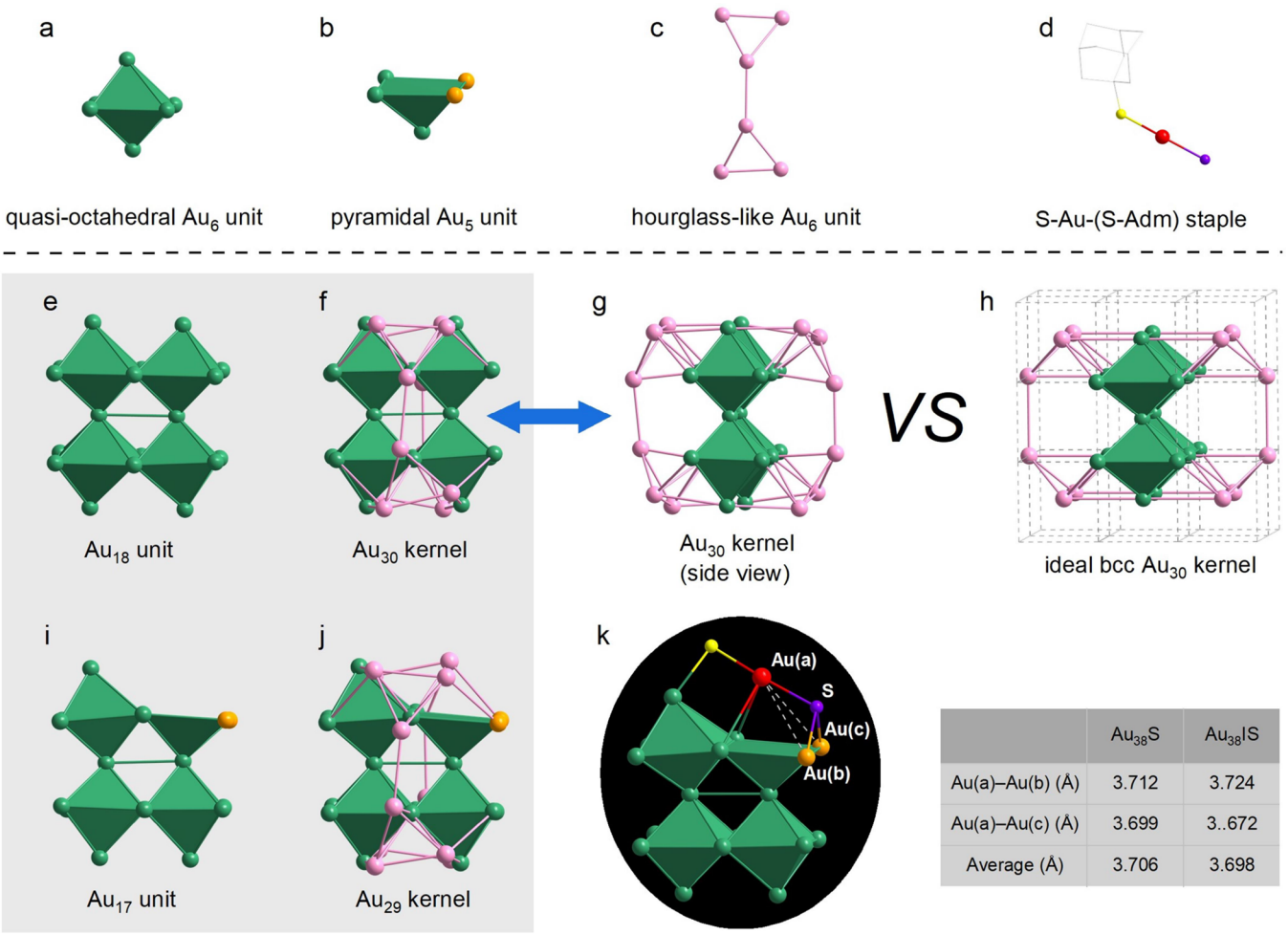

	$Au_{38}S$	$Au_{38}IS$
Au(a)–Au(b) (Å)	3.712	3.724
Au(a)–Au(c) (Å)	3.699	3..672
Average (Å)	3.706	3.698

Figure 2. Au_{30} and Au_{29} kernels of the three Au_{38} NCs. (a) Quasi-octahedral Au_6 unit; (b) pyramidal Au_5 unit; (c) hourglass-like Au_6 unit; (d) AuS(S-Adm) "staple"; (e) Au_{18} unit of $Au_{38}I$ NCs; (f) Au_{30} kernel of $Au_{38}I$ NCs; (g) side view of Au_{30} kernel; (h) ideal bcc Au_{30} kernel; (i) Au_{17} unit of $Au_{38}S$ and $Au_{38}IS$ NCs; (j) Au_{29} kernel of $Au_{38}S$ and $Au_{38}IS$ NCs; (k) Au(a)−Au(b); and Au(a)−Au(c) distances of $Au_{38}S$ and $Au_{38}IS$. For clarity, all C and H atoms are omitted. Yellow and purple denote S, gray denotes C, and the other colors denote Au.

details). Finally, the single S-adduct $Au_{38}IS(S\text{-}Adm)_{19}$ ($Au_{38}IS$ for short) was synthesized by the additional introduction of $Cd(NO_3)_2{\cdot}4H_2O$. The molecular composition of $Au_{38}I$ was identified by electrospray ionization mass spectrometry (ESI-MS) and further confirmed by single-crystal X-ray crystallography (SCXC). As shown in Figure S1a, one dominant ion peak at m/z 5527.67 was readily assigned to $[Au_{38}I(S\text{-}Adm)_{19} + 2Cs]^{2+}$ (to assist ionization, cesium acetate (CsOAc) was added to the NC solution to form $[cluster + xCs]^{x+}$ adducts before ESI-MS analysis), indicating that the single I doping was achieved on the gold NC surface. NC neutrality was evidenced by the equal numbers of Cs^+ and ion charge, as well as by the absence of a rational signal without the addition of Cs^+. Likewise, ESI-MS analysis revealed the compositions of $Au_{38}S$ and $Au_{38}IS$, with dominant peaks at m/z 5564.66 and m/z 5543.88 readily assigned to $[Au_{38}S(S\text{-}Adm)_{20} + 2Cs]^{2+}$ and $[Au_{38}IS(S\text{-}Adm)_{19} + 2Cs]^{2+}$, respectively, see Figure S1b,c, indicating successful single S replacement and addition on the $Au_{38}I$ surface. The elemental composition of the three Au_{38} NCs was further confirmed by X-ray photoelectron spectroscopy (XPS) and energy dispersive spectrometry (EDS) elemental mapping (Figures S2−S4).

Detailed structural information on the three Au_{38} NCs was revealed by SCXC analysis, confirming the successful achievement of successive single nonmetal atom doping, replacement, and addition on the gold NC surface. Compared with the reported $Au_{38}S_2(S\text{-}Adm)_{20}$[53] (Figure S5), the three as-obtained NCs possessed a more complete 3 × 3 × 2 bcc array of kernel atoms. For comparison, the three NCs were disassembled into "kernels" and "staples" (Figures 2 and S5). As shown in Figure 2e−k, $Au_{38}I$ contained an Au_{30} bcc kernel, while the other two NCs contained Au_{29} kernels with incomplete bcc arrays. The Au_{30} kernel of $Au_{38}I$ consisted of two hourglass-like Au_6 units (marked in pink) and one regular 3 × 2 × 1 bcc Au_{18} unit (consisting of four quasi-octahedral Au_6 units sharing six Au atoms) (Figure 2f). The Au−Au bond lengths of the hourglass-like Au_6 unit and the Au_{18} unit were 2.84 and 2.75 Å, respectively, and the average Au−Au distance between the Au_{18} unit and the hourglass-like Au_6 unit was 2.85 Å. Both $Au_{38}S$ and $Au_{38}IS$ possessed similar Au_{29} kernels, which consisted of two hourglass-like Au_6 units and one 3 × 2 × 1 bcc Au_{17} unit (composed of three quasi-octahedral Au_6 units and one pyramidal Au_5 unit by sharing six Au atoms) (Figure 2k). The average Au−Au bond lengths of the Au_{17} units in $Au_{38}S$ and $Au_{38}IS$ were both 2.86 Å, and the average Au−Au distances between the Au_{17} unit and the hourglass-like Au_6 unit in $Au_{38}S$ and $Au_{38}IS$ were 2.86 and 2.87 Å, respectively. The integrality of the bcc array endowed Au_{38} NCs with structural

https://doi.org/10.1021/jacs.3c13635
J. Am. Chem. Soc. 2024, 146, 9026−9035

stability, which was consistent with the observation that the thermostability of $Au_{38}I$ was higher than that of $Au_{38}S$ and $Au_{38}IS$ (Figure S6).

The pyramidal Au_5 unit served as the skeleton of the quasi-octahedral Au_6 unit, which could be formed by unfolding two Au−Au bonds of the quasi-octahedral Au_6 unit through S atom doping. As shown in Figure 2k, the average distances between Au(a)−Au(b) and Au(a)−Au(c) in all pyramidal Au_5 units for $Au_{38}S$ and $Au_{38}IS$ were 3.71 and 3.70 Å, respectively, exceeding the normal Au−Au σ-bond distance,[4,55,56] and were also far longer than the corresponding Au−Au bond distances of the undoped Au_6 units ($Au_{38}I$: 2.70 Å; $Au_{38}S$: 2.72 Å; $Au_{38}IS$: 2.70 Å). These bond lengths indicated that cationized Au(a), Au(b), and Au(c) in the quasi-octahedral Au_6 unit were neutralized by the S^{2-} anion, which was supported by XPS analysis. As shown in Figure S7, the neutral Au^0 to cationic Au^{1+} ratios were 18:20 for $Au_{38}I$ and 16:22 for $Au_{38}IS$ and $Au_{38}S$, demonstrating that S atom doping degraded the integrality of the bcc kernel and counteracted the charge state of the metal atoms in the metal NCs.

The kernels of all Au_{38} NCs were selectively protected by $Au_2(S\text{-}Adm)_3$, AuS(S-Adm), S-Adm, and I. Specifically, four $Au_2(S\text{-}Adm)_3$ units, seven bridging S-Adm molecules, and one I atom shielded the Au_{30} kernel of $Au_{38}I$ (Figure S5a−d). Two hourglass-like Au_6 units of the Au_{30} kernel were separately immobilized by two $Au_2(S\text{-}Adm)_3$ "staples", with an average Au−Au bond length of 2.80 Å and an average Au−S−Au bond angle of 91.60°. All quasi-octahedral Au_6 units were bridged and stabilized by an independent S-Adm molecule and I atom, with an average Au−S bond length of 2.38 Å and a Au−I bond length of 2.74 Å. $Au_{38}S$ and $Au_{38}IS$ possessed the same Au_{29} kernel. For $Au_{38}S$, the Au_{29} kernel was capped by an outer shell consisting of one AuS(S-Adm) unit, four $Au_2(S\text{-}Adm)_3$ units, and six S-Adm molecules; For $Au_{38}IS$, the components of the outer shell were similar to those of $Au_{38}S$, except that one S-Adm molecule was replaced by one I atom (Figure S5f−i). Especially, as illustrated in Figure 2k, one AuS(S-Adm) unit was located on the quasi-octahedral Au_6 unit and the pyramidal Au_5 unit reinforcing the connection between them and resulting in the short Au−(S-Adm) bond lengths of 2.34 Å for $Au_{38}S$ and 2.32 Å for $Au_{38}IS$. Notably, such a connector was absent in the outer shell of $Au_{38}I$. The Au−Au distances of the hourglass-like Au_6, Au_{18}, and Au_{17} units, and their distributions in $Au_{38}I$, $Au_{38}S$, and $Au_{38}IS$ are shown in Figure S8, demonstrating that the average Au−Au distances in the corresponding locations for the three NCs were nearly equal. Figure S5 displays the total structures of the three Au_{38} NCs, which clearly shows that single atom replacement of I with S, and single atom addition of S, led to the local structure change of $Au_{38}I$. $Au_{38}S$ and $Au_{38}IS$ possessed identical structural frameworks, suggesting that the single I atom, unlike the single S atom, did not significantly impact the kernel atomic structure. Note that our previous study also demonstrated that single S addition resulted in kernel structure evolution.[57] Although single atom replacement of I with S did lead to a change in the local atomic structure, it did not obviously influence the crystallographic arrangement, since both $Au_{38}I$ and $Au_{38}S$ adopted the stacking sequence of "AB" in their single crystals. Interestingly, single S addition on $Au_{38}I$ induced a crystallographic arrangement change from 2H to 4H, as seen in Figure 1b, indicating that the atomic and crystallographic structures of the metal NCs were not synchronously changed with surface single nonmetal atom replacement or addition.

Optical Properties. The electronic structures of the three Au_{38} NCs were experimentally probed by ultraviolet−visible-near-infrared (UV−Vis/NIR) spectroscopy after dissolving the crystals in CH_2Cl_2. The results indicated that the breaking of the bcc structure led to a notable blue shift in the absorption peaks. Specifically, $Au_{38}I$ with a complete bcc Au_{30} kernel exhibited two strong peaks at 558 (2.22) and 712 nm (1.74 eV) (Figure 3a), while $Au_{38}S$ and $Au_{38}IS$ with similar

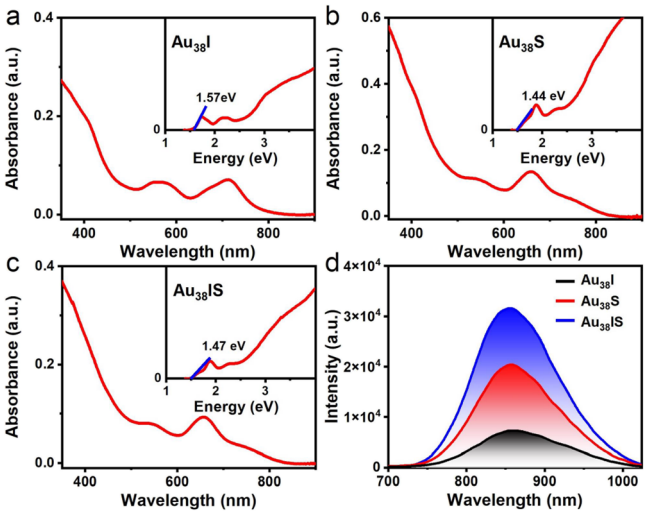

Figure 3. Absorption and PL comparisons of the three Au_{38} NCs. (a−c) UV−Vis/NIR absorption spectrum of $Au_{38}I$, $Au_{38}S$, and $Au_{38}IS$, respectively; (d) PL spectra of three Au_{38} NCs. The insets show the corresponding spectra on the energy scale.

incomplete Au_{29} kernels exhibited two strong peaks at 530 (2.34) and 659 nm (1.89 eV). $Au_{38}S$ and $Au_{38}IS$ also exhibited weak peaks at 730 (1.70) and 740 nm (1.68 eV), respectively (Figure 3b,c). By extrapolating the lowest-energy absorption peak to zero absorbance, the optical energy gaps of $Au_{38}I$, $Au_{38}S$, and $Au_{38}IS$ were determined to be ∼1.57, 1.44, and 1.47 eV, respectively. All experimental UV−Vis/NIR absorption peaks of the three Au_{38} NCs were well reproduced by time-dependent density functional theory (TD-DFT), as shown in Figures S9−S11. Kohn−Sham molecular orbital analyses revealed that the simulated peak at 532 nm for $Au_{38}I$ primarily arose from the HOMO−4 to LUMO+1 (I(p) accounting for approximately 50% of the electron transition), HOMO−1 to LUMO+3, HOMO−4 to LUMO, and HOMO−1 to LUMO +2 electronic transitions and that the peak at 650 nm arose from the HOMO−1 to LUMO+2, HOMO to LUMO+3, and HOMO to LUMO+2 electronic transitions (Figure S9). The three simulated absorption peaks of $Au_{38}S$ primarily arose from the HOMO−4 to LUMO+1, HOMO−1 to LUMO+3, HOMO−2 to LUMO+1, and HOMO to LUMO+5 electronic transitions at 460 nm, from the HOMO−2 to LUMO, HOMO−1 to LUMO, and HOMO to LUMO+3 electronic transitions at 545 nm, and from the HOMO to LUMO electronic transition at 673 nm, respectively (Figure S10). The simulated absorption of $Au_{38}IS$ exhibited three peaks, with the 450 nm peak primarily arising from the HOMO−5 to LUMO +1, HOMO to LUMO+6, and HOMO−1 to LUMO+3 electronic transitions, the 552 nm peak primarily arising from the HOMO−2 to LUMO, HOMO−1 to LUMO, and HOMO to LUMO+2 electronic transitions, and the 685 nm peak primarily arising from the HOMO to LUMO electronic

https://doi.org/10.1021/jacs.3c13635
J. Am. Chem. Soc. 2024, 146, 9026−9035

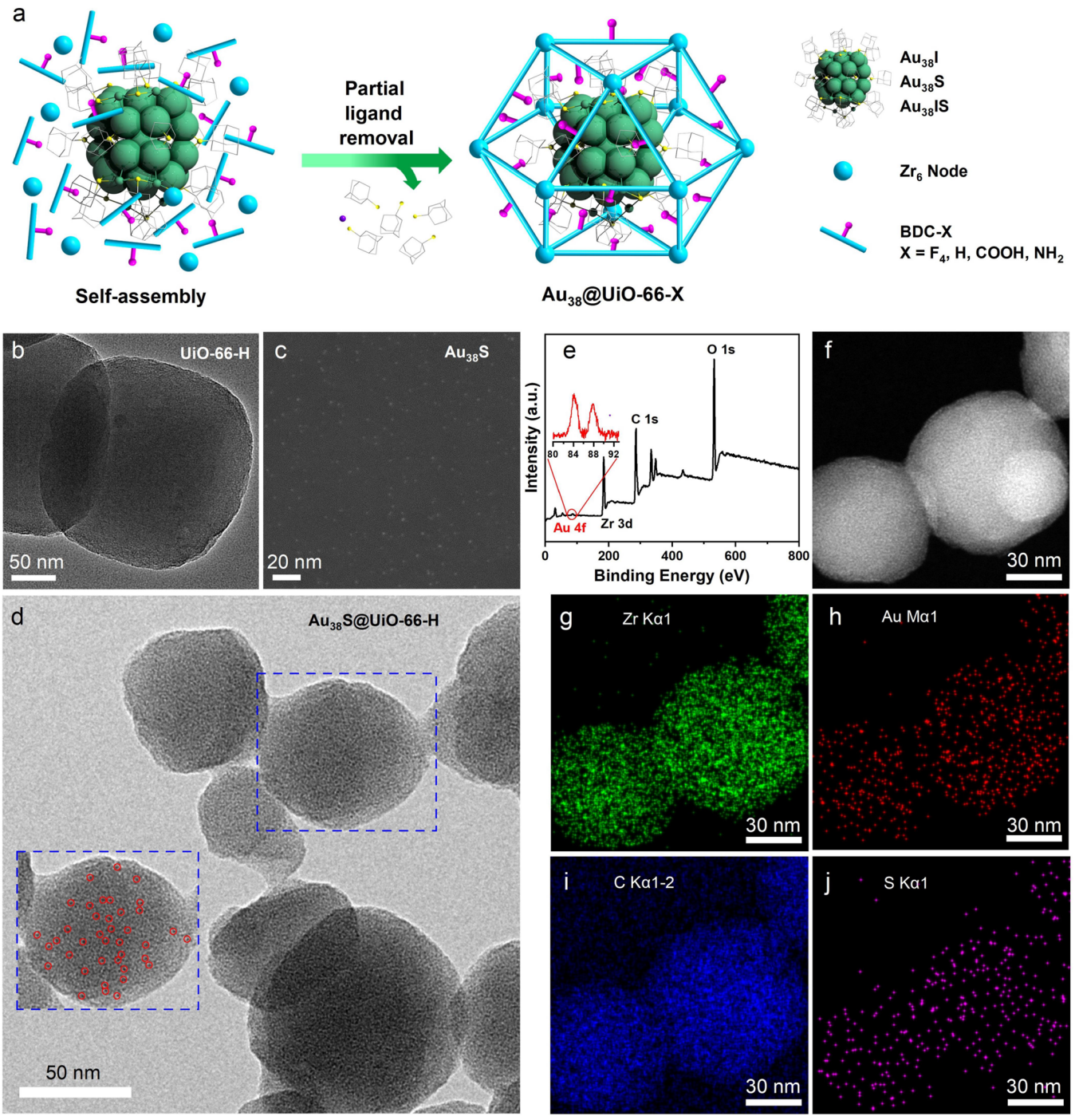

Figure 4. Synthesis and structural characterization of Au_{38}@UiO-66-X (X = F_4, H, COOH, and NH_2) composites. (a) Illustration of the synthetic route to partial-ligand-removed Au_{38}@UiO-66-X composites based on the self-assembly of Au_{38} NCs and UiO-66-X MOF precursors; (b) TEM image of UiO-66-H; (c) HAADF-STEM image of $Au_{38}S$ NCs; (d) TEM image of $Au_{38}S$@UiO-66-H composites; (e) XPS spectrum of $Au_{38}S$@UiO-66-H composites; (f–j) HADDF-STEM image and corresponding EDS elemental (Zr, Au, C, and S) mapping of $Au_{38}S$@UiO-66-H composites.

transition (Figure S11). The change in bcc kernel structure significantly affected the absorption of gold NCs, even if two NCs shared almost the same size and composition, which was consistent with cases of nonbcc gold NCs.[58−61] However, different from previous reports,[62−64] single ligand replacement of bcc NCs had almost no influence on their absorption, which indicated that the absorption of bcc gold NCs was mainly determined by the kernel rather than the protecting ligands.

All three NCs exhibited NIR photoluminescence (PL) upon excitation at 514 nm. Although their PL spectra exhibited similar profiles, the intensities differed, indicating that surface single atom replacement or addition did not notably change the radiative excitation electron transfer gap but it dramatically influenced competition between radiative and nonradiative excitation electron transfer. The quantum yield (QY) values were calculated as 2.09×10^{-4}, 6.379×10^{-4}, and 1.032×10^{-3} for $Au_{38}I$, $Au_{38}S$, and $Au_{38}IS$, respectively (Figure 3d) on the

https://doi.org/10.1021/jacs.3c13635
J. Am. Chem. Soc. 2024, 146, 9026−9035

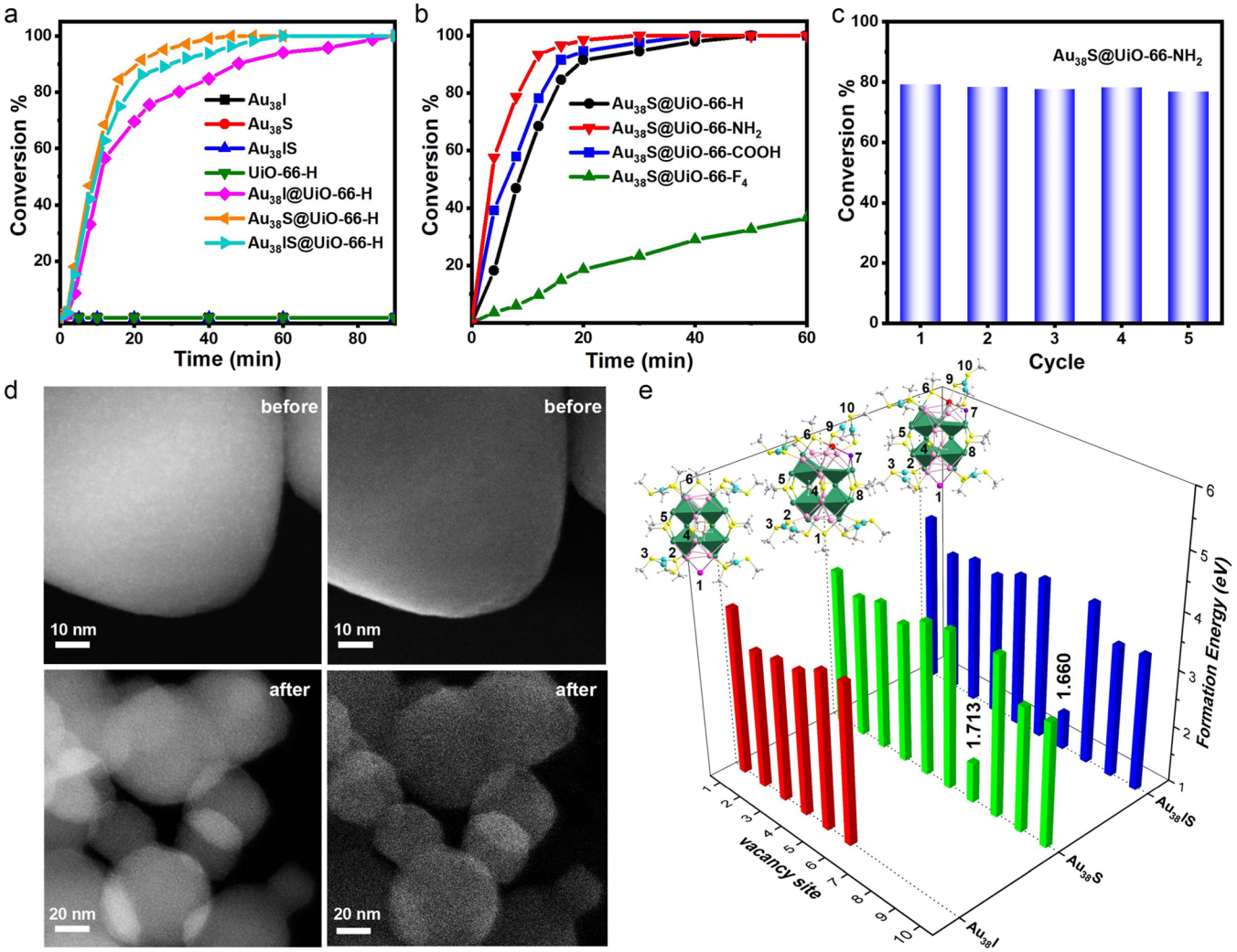

Figure 5. Catalytic performance of Au_{38}@UiO-66-X (X = F_4, H, COOH, and NH_2) composites in 4-NP reduction. (a) Catalytic performance of UiO-66-H, $Au_{38}I$, $Au_{38}S$, $Au_{38}IS$, and corresponding Au_{38}@UiO-66-H composites; (b) catalytic performance of $Au_{38}S$@UiO-66-X composites; (c) catalytic cycle of $Au_{38}S$@UiO-66-NH_2 composites; (d) HAADF-STEM (left) and SE-STEM (right) images of $Au_{38}S$@UiO-66-H before and after catalysis; (e) DFT calculation of vacancy formation energy of each site on $Au_{38}I$, $Au_{38}S$, and $Au_{38}IS$ after the removal of the S or SCH_3 ligand groups.

basis of equation[65] $Q = Q_r \times (I/I_r) \times (A_r/A) \times (\eta^2/\eta_r^2)$, where Q is the QY, A is the absorbance at the excitation wavelength, η is the average refractive index of the relevant solution, and I is the integrated area under the corrected emission spectrum for the sample (the QY of 1×10^{-4} for $Au_{25}(PET)_{18}$ was selected as the reference sample (r), Figure S12). These findings indicated that surface S atoms were more conducive to PL than I atoms and I atoms were more conducive to PL than S-Adm molecules.

Bottom-Up Construction of MOF Loricae on Au_{38} NCs. To test the bottom-up construction of MOF loricae on the NC surface, we mixed Au_{38} NCs with terephthalic acid (BDC) and zirconium (Zr) ion building blocks and successfully synthesized the composites denoted as $Au_{38}I$@UiO-66-H, $Au_{38}S$@UiO-66-H, and $Au_{38}IS$@UiO-66-H (Figures 4a and S13, see Methods for the synthesis details). The powder X-ray diffraction (XRD) patterns revealed that UiO-66-H in the composites retained its original crystallinity (Figure S14a), and UV−Vis/NIR spectroscopy indicated that the NC structure was not essentially changed in the composites (Figure S14b). Scanning electron microscopy (SEM) images demonstrated that the three Au_{38}@UiO-66-H composites possessed similar shapes and sizes (Figure S15). Transmission electron microscopy (TEM) and high-angle annular dark-field scanning TEM (HAADF-STEM) images revealed that the morphology of UiO-66-H did not change significantly, but the average size reduced from 180.1 ± 15.3 to 101.4 ± 9.5 nm in diameter (Figure S16) before and after complexing with Au_{38} NCs, which were evenly distributed inside UiO-66-H (Figures 4b−d,f, 5d, and S17). These results were further confirmed by elemental analysis via XPS and EDS for Zr, Au, C, and S as well as Au content analysis via inductively coupled plasma atomic emission spectroscopy (1.51−1.60 wt %) (Figure 4e−j and Table S1). The nitrogen sorption results indicated that the Brunauer−Emmett−Teller (BET) surface areas of $Au_{38}S$@UiO-66-H, $Au_{38}IS$@UiO-66-H, and $Au_{38}I$@UiO-66-H were 1131, 1133, and 1151 m^2/g, respectively, reflecting the close cavity occupation ratios in the three composites (Figure S18a,c).

After the successful construction of MOFs on the metal NC surface, the catalytic performance of the composites in the reduction of *p*-nitrophenol (4-NP) was investigated. Although

https://doi.org/10.1021/jacs.3c13635
J. Am. Chem. Soc. 2024, 146, 9026−9035

the three Au_{38} NCs were unable to catalyze the reduction reaction alone, as monitored by UV−Vis/NIR spectroscopy (Figures S19a−c and S20a,b), their composites exhibited considerable activity, following the order of $Au_{38}S$@UiO-66-H > $Au_{38}IS$@UiO-66-H > $Au_{38}I$@UiO-66-H (Figures 5a and S21). XRD and UV−Vis/NIR spectroscopy of the three composites did not show any obvious change before and after catalysis (Figure S14c,d), indicating that the composites (including metal NCs and UiO-66-H) retained structural integrity. From HAADF-STEM and SE-STEM images, no particles can be observed, which revealed that Au_{38} NCs might be encapsulated in UiO-66-H without notable leakage or aggregation (Figure 5d). To exclude the influence of UiO-66-H, we tested the catalytic performance of UiO-66-H alone, observing no catalytic activity. Contact angle measurements indicated that the three composites were hydrophilic to a certain extent (Figure S22a−c), which inspired us to tune the catalytic activity by modifying the water solubility of the MOF sheath. To achieve this, we modified the functional group of UiO-66 and constructed the MOF in situ on the $Au_{38}S$ surface. Three functionalized composites were successfully obtained, namely, $Au_{38}S$@UiO-66-NH_2, $Au_{38}S$@UiO-66-COOH, and $Au_{38}S$@UiO-66-F_4 (see Methods for synthesis details). XRD and UV−Vis/NIR spectroscopy revealed that the three functionalized UiO-66 MOFs and $Au_{38}S$ NCs were essentially unaltered after complexing (Figure S23a,b). SEM images indicated that $Au_{38}S$ NCs were encapsulated inside UiO-66-X with similar shapes and sizes (Figure S24). HAADF-STEM and SE-STEM images clearly revealed that $Au_{38}S$ remained uniformly inside the MOF in the investigated $Au_{38}S$@UiO-66-NH_2 (Figure S25a,b). The BET surface areas of $Au_{38}S$@UiO-66-X (X = NH_2, COOH, and F_4) were investigated by nitrogen adsorption at 77 K (Figure S18b,d), which indicated that the decrease in BET surface area after the introduction of different functional groups was attributed to the MOF functional group occupying part of the pore volume. Contact angle measurements indicated that $Au_{38}S$@UiO-66-F_4 was hydrophobic, while the other three composites were hydrophilic. The hydrophilicity, as displayed in Figure S22, was in the order of $Au_{38}S$@UiO-66-NH_2 > $Au_{38}S$@UiO-66-COOH > $Au_{38}S$@UiO-66-H > $Au_{38}S$@UiO-66-F_4. Initially, the catalytic activity of the three functionalized UiO-66 MOFs toward 4-NP reduction was examined, as shown in Figure S19d−f. The influence of defective UiO-66-X (defective UiO-66-NH_2, for example) was also investigated, given the possible generation of defects during encapsulation of Au_{38} NCs (Figure S20c,d). Subsequently, the catalytic performance of functionalized $Au_{38}S$@UiO-66-X was evaluated, revealing that hydrophilic $Au_{38}S$@UiO-66-NH_2 and $Au_{38}S$@UiO-66-COOH possessed remarkable catalytic activity and completely catalyzed the conversion of 4-NP within 30 and 40 min, respectively. In contrast, hydrophobic $Au_{38}S$@UiO-66-F_4 could catalyze only 40% 4-NP conversion within 1 h (Figures 5b and S26). The catalytic activity of the functionalized composites was in the order $Au_{38}S$@UiO-66-NH_2 > $Au_{38}S$@UiO-66-COOH > $Au_{38}S$@UiO-66-H > $Au_{38}S$@UiO-66-F_4, which was consistent with the hydrophilicity order, indicating that composite catalytic activity was positively related to the MOF lorica hydrophilicity and could be enhanced by improving the MOF water solubility. Note that, the introduction of functional groups can change the pore size of MOFs as shown in Figure S18, however, the pore sizes are not regularly correlated to the catalytic activity of the composites, indicating that such an influencing factor is not the major one in our case. The catalytic stability of three additional $Au_{38}S$@UiO-66-X composites was assessed by XRD, UV−Vis/NIR, HAADF-STEM, and SE-STEM analyses of recycled samples (Figures S23c,d and S25c,d), which demonstrated an almost unchanged conversion rate of 4-NP (∼77%) after five catalytic cycles. These findings demonstrated that constructing MOF loricae on the metal NC surface is an efficient way to improve the catalytic activity and stability of metal NCs, and both MOF and metal NC surface tailoring can sensitively influence the catalytic performance of the composite.

Catalytic Mechanism. We conjectured that the introduction of single nonmetal atom ligands might affect the catalytic performance of surface-tailored metal NCs. Although we did not detect free S and I species in the catalyzed reaction mixture, surprisingly we found the free thiolates via gas chromatography (GC) and mass spectrometry (MS) (Figure S27) in the extracted reaction mixture when synthesizing Au_{38}@UiO-66 composites. This finding indicated thiolate loss during the MOF construction on the NC surface, which was not previously reported and might be responsible for the improved catalytic activity of metal NCs. Quantified calculations revealed that $Au_{38}S$, $Au_{38}IS$, and $Au_{38}I$ lost ∼5, 4, and 1 thiolates, respectively (Tables S2 and S3), and the order of thiolate removal was consistent with the order of catalytic activity ($Au_{38}S$ > $Au_{38}IS$ > $Au_{38}I$), providing evidence for the enhanced catalytic activity. DFT calculations of vacancy formation energy (VFE) revealed that the lowest three VFEs of thiolates were 3.19, 3.20, and 3.47 eV for $Au_{38}S$; 3.35, 3.40, and 3.49 eV for $Au_{38}IS$; and 3.41, 3.49, and 3.54 eV for $Au_{38}I$, respectively as shown in Figures 5e and S28, and Table S4. These results indicated that $Au_{38}S$ could lose more thiolates than $Au_{38}IS$; however, the latter could lose more thiolates than $Au_{38}I$ within the energy limits, providing an explanation for the experimental results. Notably, the single nonmetal S atom in $Au_{38}S$ and $Au_{38}IS$ was easier to lose than a thiolate, whereas the I atom in $Au_{38}I$ and $Au_{38}IS$ was more difficult to lose. The easy loss of the S atom might be related to the fact that the resulting structures were more bcc-complete with relatively low energies (Figure S29). Unfortunately, S was not detected by GC-MS due to its ultralow content or serious interference from thiolates. The NCs remained stable after partial ligand removal (including thiolates and S), as monitored by UV−Vis/NIR spectrometry, XRD, SEM, and TEM, as mentioned above, providing evidence that surface MOF construction is an efficient strategy for protecting NCs.

■ CONCLUSIONS

Herein, we developed a synthesis method that enabled the realization of challenging single nonmetal atom doping, replacement, and addition on the metal NC surface, and we successfully synthesized and precisely characterized three novel NCs: $Au_{38}I$, $Au_{38}S$, and $Au_{38}IS$. $Au_{38}I$ and $Au_{38}S$ possessed slightly different atomic structures but similar 2H crystallographic arrangements, while $Au_{38}IS$ and $Au_{38}S$ possessed similar atomic structures but different crystallographic arrangements, indicating that I and S atoms had different influences on the atomic and crystallographic structures of metal NCs, which were not synchronously changed. $Au_{38}S$ and $Au_{38}IS$ exhibited almost identical absorption profiles, but $Au_{38}I$ showed slightly shifted absorption profiles, indicating that the UV−Vis/NIR spectra of metal NCs were correlated to their structures. $Au_{38}I$, $Au_{38}S$, and $Au_{38}IS$ exhibited similar PL profiles; however, their

https://doi.org/10.1021/jacs.3c13635
J. Am. Chem. Soc. 2024, 146, 9026−9035

QY values followed the order $Au_{38}IS$ > $Au_{38}S$ > $Au_{38}I$, indicating that their PL profiles were not sensitive to their atomic structures. I or S introduction did not notably change the radiative excitation electron transfer gap but obviously influenced the competition between radiative and nonradiative excitation electron transfer, and the ligand contributions to PL followed the order of S > I > S-Adm. Furthermore, MOFs were constructed on the NC surface by a bottom-up method. Although surface MOF construction did not essentially alter the metal NC structure, it led to the partial release of ligands and stimulated the catalytic activity of metal NCs, which was not previously reported. NC surface tailoring and MOF functional group modification efficiently impacted the catalytic activity of metal NCs, indicating new ways to modify the properties of metal NCs after coating with MOFs. The surface MOF acted as a lorica to protect the NC and enhanced its water solubility, which is significant for catalysis in the aqueous phase. Thus, the findings in this work have important implications for structure (composition) and property tailoring, providing insights into the structure (composition)−property correlation of metal NCs that is expected to stimulate more research in related fields.

■ ASSOCIATED CONTENT

Supporting Information

The Supporting Information is available free of charge at https://pubs.acs.org/doi/10.1021/jacs.3c13635.

Experiment details, DFT calculation details; XPS, ESI-MS, SEM, TEM, XRD, and ICP-AES; N_2 sorption; contact angle; GC-MS; more single crystal data; and catalytic data (PDF)

Accession Codes

CCDC 2311980 and 2311982−2311983 contain the supplementary crystallographic data for this paper. These data can be obtained free of charge via www.ccdc.cam.ac.uk/data_request/cif, or by emailing data_request@ccdc.cam.ac.uk, or by contacting The Cambridge Crystallographic Data Centre, 12 Union Road, Cambridge CB2 1EZ, U.K.; Fax: +44 1223 336033.

■ AUTHOR INFORMATION

Corresponding Authors

Hai-Long Jiang − *Hefei National Research Center for Physical Sciences at the Microscale, Department of Chemistry, University of Science and Technology of China, Hefei, Anhui 230026, P. R. China;* orcid.org/0000-0002-2975-7977; Email: jianglab@ustc.edu.cn

Zhikun Wu − *Key Laboratory of Materials Physics, Anhui Key Laboratory of Nanomaterials and Nanotechnology, CAS Center for Excellence in Nanoscience, Institute of Solid State Physics, HFIPS, Chinese Academy of Sciences, Hefei, Anhui 230031, P. R. China; Institute of Physical Science and Information Technology, Anhui University, Hefei, Anhui 230601, P. R. China;* orcid.org/0000-0002-2711-3860; Email: zkwu@issp.ac.cn

Authors

Qing You − *Key Laboratory of Materials Physics, Anhui Key Laboratory of Nanomaterials and Nanotechnology, CAS Center for Excellence in Nanoscience, Institute of Solid State Physics, HFIPS, Chinese Academy of Sciences, Hefei, Anhui 230031, P. R. China; Institute of Physical Science and Information Technology, Anhui University, Hefei, Anhui 230601, P. R. China*

He Wang − *Hefei National Research Center for Physical Sciences at the Microscale, Department of Chemistry, University of Science and Technology of China, Hefei, Anhui 230026, P. R. China*

Yan Zhao − *Key Laboratory of Materials Physics, Anhui Key Laboratory of Nanomaterials and Nanotechnology, CAS Center for Excellence in Nanoscience, Institute of Solid State Physics, HFIPS, Chinese Academy of Sciences, Hefei, Anhui 230031, P. R. China; Institute of Physical Science and Information Technology, Anhui University, Hefei, Anhui 230601, P. R. China*

Wentao Fan − *Key Laboratory of Materials Physics, Anhui Key Laboratory of Nanomaterials and Nanotechnology, CAS Center for Excellence in Nanoscience, Institute of Solid State Physics, HFIPS, Chinese Academy of Sciences, Hefei, Anhui 230031, P. R. China; Institute of Physical Science and Information Technology, Anhui University, Hefei, Anhui 230601, P. R. China;* orcid.org/0000-0003-0806-9558

Wanmiao Gu − *Key Laboratory of Materials Physics, Anhui Key Laboratory of Nanomaterials and Nanotechnology, CAS Center for Excellence in Nanoscience, Institute of Solid State Physics, HFIPS, Chinese Academy of Sciences, Hefei, Anhui 230031, P. R. China; Institute of Physical Science and Information Technology, Anhui University, Hefei, Anhui 230601, P. R. China*

Complete contact information is available at: https://pubs.acs.org/10.1021/jacs.3c13635

Author Contributions

‖These authors contributed equally.

Notes

The authors declare no competing financial interest.

■ ACKNOWLEDGMENTS

This work was supported by the National Natural Science Foundation of China (Nos. 22331009, 21925303, 21829501, 22033005, 22038002, 22103035, 21771186, 21222301, 22075290, 21171170, and 21528303), the National Key Research and Development Project (Grant No. 2021YFA1500402), the Strategic Priority Research Program of the CAS (XDB0450302, XDB0540000), the CASHIPS Director's Fund (BJPY2019A02), the Innovative Program of Development Foundation of Hefei Center for Physical Science and Technology (2020HSC−CIP005, 2022HSC−CIP018), and the Foundation of President of HFIPS (YZJJ202306-TS, YZJJ-GGZX-2022-01).

■ REFERENCES

(1) Li, G.; Jin, R. Atomically precise gold nanoclusters as new model catalysts. *Acc. Chem. Res.* **2013**, *46*, 1749−1758.

(2) Zhang, L.; Wang, E. Metal nanoclusters: New fluorescent probes for sensors and bioimaging. *Nano Today* **2014**, *9*, 132−157.

(3) Fang, J.; Zhang, B.; Yao, Q.; Yang, Y.; Xie, J.; Yan, N. Recent advances in the synthesis and catalytic applications of ligand-protected, atomically precise metal nanoclusters. *Coord. Chem. Rev.* **2016**, *322*, 1−29.

(4) Chakraborty, I.; Pradeep, T. Atomically precise clusters of noble metals: Emerging link between atoms and nanoparticles. *Chem. Rev.* **2017**, *117*, 8208−8271.

(5) Du, Y.; Sheng, H.; Astruc, D.; Zhu, M. Atomically precise noble metal nanoclusters as efficient catalysts: A bridge between structure and properties. *Chem. Rev.* **2020**, *120*, 526−622.
(6) Jin, Y.; Zhang, C.; Dong, X.-Y.; Zang, S.-Q.; Mak, T. C. W. Shell engineering to achieve modification and assembly of atomically-precise silver clusters. *Chem. Soc. Rev.* **2021**, *50*, 2297−2319.
(7) Liu, D.; Du, W.; Chen, S.; Kang, X.; Chen, A.; Zhen, Y.; Jin, S.; Hu, D.; Wang, S.; Zhu, M. Interdependence between nanoclusters $AuAg_{24}$ and Au_2Ag_{41}. *Nat. Commun.* **2021**, *12*, No. 778.
(8) Xia, N.; Xing, J.; Peng, D.; Ji, S.; Zha, J.; Yan, N.; Su, Y.; Jiang, X.; Zeng, Z.; Zhao, J.; Wu, Z. Assembly-induced spin transfer and distance-dependent spin coupling in atomically precise AgCu nanoclusters. *Nat. Commun.* **2022**, *13*, No. 5934.
(9) Seong, H.; Choi, M.; Park, S.; Kim, H.-W.; Kim, J.; Kim, W.; Yoo, J. S.; Lee, D. Promoting CO_2-to-CO electroreduction via the active-site engineering of atomically precise silver nanoclusters. *ACS Energy Lett.* **2022**, *7*, 4177−4184.
(10) Suyama, M.; Takano, S.; Tsukuda, T. Spontaneous intercluster electron transfer $X^{2-} + X^0 \rightarrow 2\ X^-$ ($X = PtAu_{24}(SC_nH_{2n+1})_{18}$) in solution: Promotion by long alkyl chains. *J. Am. Chem. Soc.* **2023**, *145*, 3361−3368.
(11) Li, G.; Hou, J.; Lei, X.; Li, D.; Yu, E.; Hu, W.; Cai, X.; Liu, X.; Chen, M.; Zhu, Y. Reactivity and recyclability of ligand-protected metal cluster catalysts for CO_2 transformation. *Angew. Chem., Int. Ed.* **2023**, *62*, No. e202216735.
(12) Wang, X.; Yin, B.; Jiang, L.; Yang, C.; Liu, Y.; Zou, G.; Chen, S.; Zhu, M. Ligand-protected metal nanoclusters as low-loss, highly polarized emitters for optical waveguides. *Science* **2023**, *381*, 784−790.
(13) Ma, F.; Abboud, K. A.; Zeng, C. Precision synthesis of a CdSe semiconductor nanocluster via cation exchange. *Nat. Synth.* **2023**, *2*, 949−959.
(14) Lee, W.; Smith, A. M. Magic reactions transform nanoclusters. *Nat. Synth.* **2023**, *2*, 904−905.
(15) Jin, S.; Du, W.; Wang, S.; Kang, X.; Chen, M.; Hu, D.; Chen, S.; Zou, X.; Sun, G.; Zhu, M. Thiol-induced synthesis of phosphine-protected gold nanoclusters with atomic precision and controlling the structure by ligand/metal engineering. *Inrog. Chem.* **2017**, *56*, 11151−11159.
(16) Li, Q.; Luo, T.-Y.; Taylor, M. G.; Wang, S.; Zhu, X.; Song, Y.; Mpourmpakis, G.; Rosi, N. L.; Jin, R. Molecular "surgery" on a 23-gold-atom nanoparticle. *Sci. Adv.* **2017**, *3*, No. e1603193.
(17) Ren, L.; Yuan, P.; Su, H.; Malola, S.; Lin, S.; Tang, Z.; Teo, B. K.; Häkkinen, H.; Zheng, L.; Zheng, N. Bulky surface ligands promote surface reactivities of $[Ag_{141}X_{12}(S\text{-}Adm)_{40}]^{3+}$ (X = Cl, Br, I) nanoclusters: models for multiple-twinned nanoparticles. *J. Am. Chem. Soc.* **2017**, *139*, 13288−13291.
(18) Wan, X.-K.; Cheng, X.-L.; Tang, Q.; Han, Y.-Z.; Hu, G.; Jiang, D.-E.; Wang, Q.-M. Atomically precise bimetallic $Au_{19}Cu_{30}$ nanocluster with an icosidodecahedral Cu_{30} shell and an alkynyl−Cu interface. *J. Am. Chem. Soc.* **2017**, *139*, 9451−9454.
(19) Kang, X.; Xiang, J.; Lv, Y.; Du, W.; Yu, H.; Wang, S.; Zhu, M. Synthesis and structure of self-assembled $Pd_2Au_{23}(PPh_3)_{10}Br_7$ nanocluster: Exploiting factors that promote assembly of icosahedral nanobuilding-blocks. *Chem. Mater.* **2017**, *29*, 6856−6862.
(20) Higaki, T.; Liu, C.; Zhou, M.; Luo, T.-Y.; Rosi, N. L.; Jin, R. Tailoring the structure of 58-electron gold nanoclusters: $Au_{103}S_2(S\text{-}Nap)_{41}$ and its implications. *J. Am. Chem. Soc.* **2017**, *139*, 9994−10001.
(21) Zhang, S.-S.; Feng, L.; Senanayake, R. D.; Aikens, C. M.; Wang, X.-P.; Zhao, Q.-Q.; Tung, C.-H.; Sun, D. Diphosphine-protected ultrasmall gold nanoclusters: opened icosahedral Au_{13} and heart-shaped Au_8 clusters. *Chem. Sci.* **2018**, *9*, 1251−1258.
(22) Shen, X.-T.; Ma, X.-L.; Ni, Q.-L.; Ma, M.-X.; Gui, L.-C.; Hou, C.; Hou, R.-B.; Wang, X.-J. $[Ag_{15}(N\text{-triphos})_4(Cl_4)](NO_3)_3$: a stable Ag−P superatom with eight electrons (N-triphos = tris-((diphenylphosphino)methyl)amine). *Nanoscale* **2018**, *10*, 515−519.
(23) Johnson, G.; Yang, M. Y.; Liu, C.; Zhou, H.; Zuo, X.; Dickie, D. A.; Wang, S.; Gao, W.; Anaclet, B.; Perras, F. A.; Ma, F.; Zeng, C.; Wang, D.; Bals, S.; Dai, S.; Xu, Z.; Liu, G.; Goddard, W. A.; Zhang, S. Nanocluster superstructures assembled via surface ligand switching at high temperature. *Nat. Synth.* **2023**, *2*, 828−837.
(24) Li, Z.; Liu, C.; Abroshan, H.; Kauffman, D. R.; Li, G. $Au_{38}S_2(SAdm)_{20}$ photocatalyst for one-step selective aerobic oxidations. *ACS Catal.* **2017**, *7*, 3368−3374.
(25) Higaki, T.; Li, Y.; Zhao, S.; Li, Q.; Li, S.; Du, X. S.; Yang, S.; Chai, J.; Jin, R. Atomically tailored gold nanoclusters for catalytic application. *Angew. Chem., Int. Ed.* **2019**, *58*, 8291−8302.
(26) Jin, R.; Li, G.; Sharma, S.; Li, Y.; Du, X. Toward active-site tailoring in heterogeneous catalysis by atomically precise metal nanoclusters with crystallographic structures. *Chem. Rev.* **2021**, *121*, 567−648.
(27) Wan, X.-K.; Wang, J.-Q.; Wang, Q.-M. Ligand-protected Au_{55} with a novel structure and remarkable CO_2 electroreduction performance. *Angew. Chem., Int. Ed.* **2021**, *60*, 20748−20753.
(28) Zhao, H.; You, Q.; Zhu, W.; Li, J.; Deng, H.; Li, M.-B.; Zhao, Y.; Wu, Z. Nanoclusterzyme for dual colorimetric sensings: A case study on $[Au_{14}(Dppp)_5I_4]^{2+}$. *Small* **2023**, *19*, No. 2207936.
(29) Zhou, H. C.; Long, J. R.; Yaghi, O. M. Introduction to metal-organic frameworks. *Chem. Rev.* **2012**, *112*, 673−674.
(30) Furukawa, H.; Cordova, K. E.; O'Keeffe, M.; Yaghi, O. M. The chemistry and applications of metal-organic frameworks. *Science* **2013**, *341*, No. 1230444.
(31) Zhou, H. C.; Kitagawa, S. Metal-organic frameworks (MOFs). *Chem. Soc. Rev.* **2014**, *43*, 5415−5418.
(32) Dhakshinamoorthy, A.; Garcia, H. Catalysis by metal nanoparticles embedded on metal−organic frameworks. *Chem. Soc. Rev.* **2012**, *41*, 5262−5284.
(33) Moon, H. R.; Lim, D.-W.; Suh, M. P. Fabrication of metal nanoparticles in metal−organic frameworks. *Chem. Soc. Rev.* **2013**, *42*, 1807−1824.
(34) Zhao, M.; Yuan, K.; Wang, Y.; Li, G.; Guo, J.; Gu, L.; Hu, W.; Zhao, H.; Tang, Z. Metal−organic frameworks as selectivity regulators for hydrogenation reactions. *Nature* **2016**, *539*, 76−80.
(35) Yang, Q.; Xu, Q.; Jiang, H. L. Metal-organic frameworks meet metal nanoparticles: synergistic effect for enhanced catalysis. *Chem. Soc. Rev.* **2017**, *46*, 4774−4808.
(36) Huang, R. W.; Wei, Y. S.; Dong, X. Y.; Wu, X. H.; Du, C. X.; Zang, S. Q.; Mak, T. C. W. Hypersensitive dual-function luminescence switching of a silver-chalcogenolate cluster-based metal-organic framework. *Nat. Chem.* **2017**, *9*, 689−697.
(37) Wang, Q.; Astruc, D. State of the art and prospects in metal−organic framework (MOF)-based and MOF-derived nanocatalysis. *Chem. Rev.* **2020**, *120*, 1438−1511.
(38) Kollmannsberger, K. L.; Kronthaler, L.; Jinschek, J. R.; Fischer, R. A. Defined metal atom aggregates precisely incorporated into metal−organic frameworks. *Chem. Soc. Rev.* **2022**, *51*, 9933−9959.
(39) Zhao, Y.; Zhuang, S.; Liao, L.; Wang, C.; Xia, N.; Gan, Z.; Gu, W.; Li, J.; Deng, H.; Wu, Z. A dual purpose strategy to endow gold nanoclusters with both catalysis activity and water solubility. *J. Am. Chem. Soc.* **2020**, *142*, 973−977.
(40) Liu, C.; Zeng, C.; Luo, T.-Y.; Merg, A. D.; Jin, R.; Rosi, N. L. Establishing porosity gradients within metal−organic frameworks using partial postsynthetic ligand exchange. *J. Am. Chem. Soc.* **2016**, *138*, 12045−12048.
(41) Luo, Y.; Fan, S.; Yu, W.; Wu, Z.; Cullen, D. A.; Liang, C.; Shi, J.; Su, C. Fabrication of $Au_{25}(SG)_{18}$-ZIF-8 nanocomposites: A facile strategy to position $Au_{25}(SG)_{18}$ nanoclusters inside and outside ZIF-8. *Adv. Mater.* **2018**, *30*, No. 1704576.
(42) Yun, Y.; Fang, Y.; Fu, W.; Du, W.; Zhu, Y.; Sheng, H.; Astruc, D.; Zhu, M. Exploiting the fracture in metal-organic frameworks: A general strategy for bifunctional atom-precise nanocluster/ZIF-8(300 °C) composites. *Small* **2022**, *18*, No. e2107459.
(43) Luo, L.; Jin, R. Atomically precise metal nanoclusters meet metal-organic frameworks. *iScience* **2021**, *24*, No. 103206.
(44) Kratzl, K.; Kratky, T.; Gunther, S.; Tomanec, O.; Zboril, R.; Michalicka, J.; Macak, J. M.; Cokoja, M.; Fischer, R. A. Generation

https://doi.org/10.1021/jacs.3c13635
J. Am. Chem. Soc. 2024, 146, 9026−9035

and stabilization of small platinum clusters $Pt_{12\pm x}$ inside a metal-organic framework. *J. Am. Chem. Soc.* **2019**, *141*, 13962−13969.
(45) Yun, Y.; Sheng, H.; Bao, K.; Xu, L.; Zhang, Y.; Astruc, D.; Zhu, M. Design and remarkable efficiency of the robust sandwich cluster composite nanocatalysts ZIF-8@Au_{25}@ZIF-67. *J. Am. Chem. Soc.* **2020**, *142*, 4126−4130.
(46) Zhu, Y.; Qiu, X.; Zhao, S.; Guo, J.; Zhang, X.; Zhao, W.; Shi, Y.; Tang, Z. Structure regulated catalytic performance of gold nanocluster-MOF nanocomposites. *Nano Res.* **2020**, *13*, 1928−1932.
(47) Zheng, F.; Fan, Y.; Chen, W. Homogeneous distribution of $Pt_{16}(C_4O_4SH_5)_{26}$ clusters in ZIF-67 for efficient hydrogen generation and oxygen reduction. *ACS Appl. Mater. Interfaces* **2021**, *13*, 38170−38178.
(48) Wang, H.; Liu, X.; Yang, W.; Mao, G.; Meng, Z.; Wu, Z.; Jiang, H. L. Surface-clean Au_{25} nanoclusters in modulated microenvironment enabled by metal-organic frameworks for enhanced catalysis. *J. Am. Chem. Soc.* **2022**, *144*, 22008−22017.
(49) Zhang, J.; Cui, X.; Zhou, Y.; Kong, T.; Wang, Y.; Wei, X.; Xiong, Y. Enhancing the durability of Au clusters in CO_2 photoreduction via encapsulation in Cu-based metal−organic frameworks. *Chem. Commun.* **2023**, *59*, 2299−2302.
(50) Bi, X.; Li, L.; Niu, Q.; Liu, X.; Luo, L.; Jiang, H.; You, T. Highly fluorescent magnetic ATT-AuNCs@ZIF-8 for all-in-one detection and removal of Hg^{2+}: An ultrasensitive probe to evaluate its removal efficiency. *Inorg. Chem.* **2023**, *62*, 3123−3133.
(51) Patty, J. B.; Havenridge, S.; Tietje-Mckinney, D.; Siegler, M. A.; Singh, K. K.; Hajy Hosseini, R.; Ghabin, M.; Aikens, C. M.; Das, A. Crystal structure and optical properties of a chiral mixed thiolate/stibine-protected Au_{18} cluster. *J. Am. Chem. Soc.* **2022**, *144*, 478−484.
(52) Wei, X.; Chu, K.; Adsetts, J. R.; Li, H.; Kang, X.; Ding, Z.; Zhu, M. Nanocluster transformation induced by SbF_6^- anions toward boosting photochemical activities. *J. Am. Chem. Soc.* **2022**, *144*, 20421−20433.
(53) Liu, C.; Li, T.; Li, G.; Nobusada, K.; Zeng, C.; Pang, G.; Rosi, N. L.; Jin, R. Observation of body-centered cubic gold nanocluster. *Angew. Chem., Int. Ed.* **2015**, *54*, 9826−9829.
(54) Yang, S.; Chai, J.; Chong, H.; Song, Y.; Yu, H.; Zhu, M. Sulfonate, sulfide and thiolate ligands into an ultrasmall nanocluster: $[Ag_{40.13}Cu_{13.87}S_{19}(t\text{BuS})_{20}(t\text{BuSO}_3)_{12}]$. *Chem. Commun.* **2018**, *54*, 4314−4316.
(55) Ferrando, R.; Jellinek, J.; Johnston, R. L. Nanoalloys: From theory to applications of alloy clusters and nanoparticles. *Chem. Rev.* **2008**, *108*, 845−910.
(56) Jin, R.; Zeng, C.; Zhou, M.; Chen, Y. Atomically precise colloidal metal nanoclusters and nanoparticles: Fundamentals and opportunities. *Chem. Rev.* **2016**, *116*, 10346−10413.
(57) Gan, Z.; Chen, J.; Liao, L.; Zhang, H.; Wu, Z. Surface single-atom tailoring of a gold nanoparticle. *J. Phys. Chem. Lett.* **2018**, *9*, 204−208.
(58) Tian, S.; Li, Y. Z.; Li, M. B.; Yuan, J.; Yang, J.; Wu, Z.; Jin, R. Structural isomerism in gold nanoparticles revealed by X-ray crystallography. *Nat. Commun.* **2015**, *6*, No. 8667.
(59) Liao, L.; Zhuang, S.; Yao, C.; Yan, N.; Chen, J.; Wang, C.; Xia, N.; Liu, X.; Li, M.-B.; Li, L.; Bao, X.; Wu, Z. Structure of chiral Au_{44}(2,4-DMBT)$_{26}$ nanocluster with an 18-electron shell closure. *J. Am. Chem. Soc.* **2016**, *138*, 10425−10428.
(60) Zhuang, S.; Liao, L.; Zhao, Y.; Yuan, J.; Yao, C.; Liu, X.; Li, J.; Deng, H.; Yang, J.; Wu, Z. Is the kernel−staples match a key−lock match? *Chem. Sci.* **2018**, *9*, 2437−2442.
(61) Ghosh, A.; Mohammed, O. F.; Bakr, O. M. Atomic-level doping of metal clusters. *Acc. Chem. Res.* **2018**, *51*, 3094−3103.
(62) Das, A.; Liu, C.; Zeng, C.; Li, G.; Li, T.; Rosi, N. L.; Jin, R. Cyclopentanethiolato-protected $Au_{36}(SC_5H_9)_{24}$ nanocluster: crystal structure and implications for the steric and electronic effects of ligand. *J. Phys. Chem. A* **2014**, *118*, 8264−8269.
(63) Rambukwella, M.; Burrage, S.; Neubrander, M.; Baseggio, O.; Aprà, E.; Stener, M.; Fortunelli, A.; Dass, A. $Au_{38}(SPh)_{24}$: Au_{38} protected with aromatic thiolate ligands. *J. Phys. Chem. Lett.* **2017**, *8*, 1530−1537.
(64) Wan, X.-K.; Guan, Z.-J.; Wang, Q.-M. Homoleptic alkynyl-protected gold nanoclusters: $Au_{44}(PhC{\equiv}C)_{28}$ and $Au_{36}(PhC{\equiv}C)_{24}$. *Angew. Chem., Int. Ed.* **2017**, *56*, 11494−11497.
(65) Wong, K.-L.; Bünzli, J.-C. G.; Tanner, P. A. Quantum yield and brightness. *J. Lumin.* **2020**, *224*, No. 117256.

https://doi.org/10.1021/jacs.3c13635
J. Am. Chem. Soc. 2024, 146, 9026−9035